Deformation-Driven p-Wave Halos at the Drip Line: ^{31}Ne

T. Nakamura,[1] N. Kobayashi,[1] Y. Kondo,[1] Y. Satou,[1,2] J. A. Tostevin,[3] Y. Utsuno,[4] N. Aoi,[5] H. Baba,[5] N. Fukuda,[5] J. Gibelin,[6] N. Inabe,[5] M. Ishihara,[5] D. Kameda,[5] T. Kubo,[5] T. Motobayashi,[5] T. Ohnishi,[5] N. A. Orr,[6] H. Otsu,[5] T. Otsuka,[7] H. Sakurai,[5] T. Sumikama,[8] H. Takeda,[5] E. Takeshita,[5] M. Takechi,[5] S. Takeuchi,[5] Y. Togano,[1,5] and K. Yoneda[5]

[1]*Department of Physics, Tokyo Institute of Technology, 2-12-1 O-Okayama, Meguro, Tokyo 152-8551, Japan*
[2]*Department of Physics and Astronomy, Seoul National University, 599 Gwanak, Seoul 151-742, Republic of Korea*
[3]*Department of Physics, University of Surrey, Guildford, Surrey, GU2 7XH, United Kingdom*
[4]*Japan Atomic Energy Agency, Tokai, Ibaraki 319-1195, Japan*
[5]*RIKEN Nishina Center, Hirosawa 2-1, Wako, Saitama 351-0198, Japan*
[6]*LPC-ENSICAEN, IN2P3-CNRS et Université de Caen, F-14050, Caen Cedex, France*
[7]*Center for Nuclear Study (CNS), the University of Tokyo, Hongo, Tokyo 113-0033, Japan*
[8]*Department of Physics, Tokyo University of Science, Chiba 278-8510, Japan*

(Received 25 September 2013; revised manuscript received 14 February 2014; published 7 April 2014)

The halo structure of ^{31}Ne is studied using $1n$-removal reactions on C and Pb targets at 230 MeV/nucleon. A combined analysis of the cross sections of these nuclear and Coulomb dominated reactions that feed directly the ^{30}Ne ground-state reveals ^{31}Ne to have a small neutron separation energy, $0.15^{+0.16}_{-0.10}$ MeV, and spin-parity $3/2^-$. Consistency of the data with reaction and large-scale shell-model calculations identifies ^{31}Ne as deformed and having a significant p-wave halo component, suggesting that halos are more frequent occurrences at the neutron drip line.

DOI: 10.1103/PhysRevLett.112.142501 PACS numbers: 21.10.Gv, 21.10.Dr, 25.60.Gc, 27.30.+t

Unlike conventional atomic nuclei, whose neutron and proton distributions have similar mean radii, neutron-halo nuclei exhibit very extended distributions of one or two weakly bound neutrons outside of a compact core [1–5]. Only a small number of neutron halo nuclei have been identified, found at the limits of nuclear binding (the neutron drip line) in very light nuclei. To date, the heaviest nucleus identified as having a halolike component in its ground state is ^{31}Ne ($Z = 10$, $N = 21$). This (^{30}Ne core plus neutron) halo component in ^{31}Ne is indicated by the observations of enhanced total reaction [6] and Coulomb breakup [7] cross sections. Compared to the archetypal light $1n$-halo nuclei such as ^{11}Be and ^{19}C, with their predominant s-wave neutron plus core configurations [8–13], the properties of halo components with smaller single-particle strengths in heavier nuclei could be very different, the result of more complex mixing of configurations. As such, ^{31}Ne may provide a basis to understand emergent properties of the halo phenomenon in heavier near-drip-line nuclei.

A key question in understanding the halo phenomena is, why and in what cases is the halo favored and formed near the neutron drip line? If all atomic nuclei were spherical, and followed the conventional shell-model (SM) level ordering, the neutron halo, which requires s- or p-wave valence neutron(s) to minimize the centrifugal barrier [2,14], would be formed in only a very limited number of drip line nuclei. Hence, more prolific halo formation might signal changes of this shell structure (shell evolution) and the onset of deformation [15–17]. Specifically, when spherical symmetry is broken, the number of single-particle levels with low-ℓ components increases. Furthermore, the amplitudes of the low-ℓ components in single-particle wave functions are expected to increase with weaker neutron binding [18,19].

It is expected that ^{31}Ne is a member of the island of inversion nuclei, where deformation develops irrespective of the fact that $N \approx 20$, the spherical neutron magic number. Thus, ^{31}Ne offers a prototype system to study the mechanisms of shell evolution and deformation-driven halo formation, since the configuration of its least-bound neutron has been suggested to involve a significant s- or p-wave amplitude [6,7], as opposed to the $f_{7/2}$ dominance expected of spherical shell ordering. However, the halo component of ^{31}Ne could not be characterized quantitatively from these earlier inclusive measurements [6,7]. Neither the spin-parity (J^π) nor the shell configuration of the ground state could be confirmed there. The direct mass measurement constrained the $1n$ separation energy S_n only with large uncertainty, namely, $S_n \leq 360$ keV (1σ limit) [20].

This Letter presents a more complete characterization of the halo structure of ^{31}Ne. To disentangle this structure we introduce a method that combines $1n$-removal reactions of a fast projectile (^{31}Ne) with both a light target (C), where nuclear interactions dominate, and a heavy target (Pb), where Coulomb breakup dominates. Such $1n$-removal reactions on light target nuclei have been used to probe the single-particle and halo properties of projectiles, by measuring the cross section and momentum distribution of the residues [21]. Coulomb breakup is distinct, having

large cross sections for halo states due to enhanced low-energy electric dipole ($E1$) strengths (soft $E1$ excitation) [8,9,13,22]. We exploit these differences in the sensitivity of the nuclear and Coulomb induced $1n$-removal cross sections to the valence neutron wave functions in the projectile. The $1n$-removal cross section in the nuclear-dominated, light target reactions arises from grazing collisions and the neutron wave function near the surface of the projectile [9], while Coulomb breakup arises from impact parameters from the surface out to the adiabatic cutoff, of the order of 100 fm [8,9]. Thus, the latter cross section has stronger sensitivity to the asymptotic amplitude, S_n, and ℓ of the wave function.

We focus on the $1n$-removal partial cross sections of the two reactions that feed the ground state of the ^{30}Ne residues [^{30}Ne(0_1^+)]. This partial cross section is extracted using the γ-ray tagging method, used previously for the spectroscopy of light nuclei in both nuclear-dominated [21,23] and Coulomb-dominated [9] reactions. Assuming the ^{30}Ne core is a spectator, the partial cross section feeding the ^{30}Ne(0_1^+) state is associated with a given configuration in ^{31}Ne, with a neutron coupled to ^{30}Ne(0_1^+) with specific single-particle quantum numbers (ℓj). We also extract the inclusive parallel momentum distribution of the ^{30}Ne residues on the C target as an additional probe of these single-particle components.

The $1n$-removal cross sections of ^{31}Ne on C and Pb targets were measured at the RI-Beam Factory (RIBF) operated by the RIKEN Nishina Center and the Center for Nuclear Study (CNS), University of Tokyo. The data were taken in the experiment reported in Ref. [7], but we now incorporate, in addition, data from the γ-ray detector array DALI2. The experimental setup was identical to that in Fig. 1 of Ref. [24]. We outline the experimental setup and procedure here, including the DALI2 array.

The ^{31}Ne secondary beam was produced by fragmentation of a ^{48}Ca primary beam at 345 MeV/nucleon, and was separated through the fragment separator BigRIPS [25,26]. The A and Z of the secondary beam particle were identified event by event using the standard particle identification scheme at this facility [7]. The secondary beam bombarded the C (Pb) target of thickness 2.54 g/cm^2 (3.37 g/cm^2). The energy of ^{31}Ne at the middle of the C (Pb) target was 230 (234) MeV/nucleon. Following the reaction, the ^{30}Ne fragments were identified at the zero-degree spectrometer (ZDS). A clear separation of particle identification was obtained for both the ^{31}Ne beam and the ^{30}Ne fragment [7]. The ^{30}Ne parallel momentum in the c.m. of ^{31}Ne was extracted using the momenta obtained at BigRIPS for incoming ^{31}Ne, and at the ZDS for the outgoing ^{30}Ne, where the corresponding time of flight was used for this extraction [24].

The DALI2 γ-ray detector array, composed of 182 NaI(Tl) scintillator crystals, was installed surrounding the reaction target to detect the γ rays emitted in the deexcitation of excited ^{30}Ne residues populated in the $1n$-removal reactions.

TABLE I. $1n$-removal cross sections (σ_{-1n}) for ^{31}Ne on C and Pb targets, and the deduced Coulomb breakup cross sections [$\sigma_{-1n}(E1)$]. The three rows show the inclusive $1n$-removal cross sections, the partial cross sections feeding excited core states (^{30}Ne*) that decay through the 791 keV γ ray, and the deduced partial cross sections directly feeding ^{30}Ne(0_1^+).

	σ_{-1n}(C) (mb)	σ_{-1n}(Pb) (mb)	$\sigma_{-1n}(E1)$ (mb)
(^{31}Ne, ^{30}Ne) (Inclusive)	90(7)	720(61)	529(63)
(^{31}Ne, ^{30}Ne*)	57(13)	201(83)	81(87)
(^{31}Ne, ^{30}Ne(0_1^+))	33(15)	518(103)	448 (108)

The efficiency, estimated using standard sources and a GEANT4 code Monte Carlo simulation, was found to be 26(2)% at 662 keV in the laboratory frame. A 7% discrepancy between the simulation and the source calibration is included in the systematic uncertainty on the cross sections.

The inclusive $1n$-removal cross sections obtained on the C and Pb targets, and the Coulomb breakup cross section on the Pb target, are listed in the first row of Table I. The Coulomb breakup cross section was extracted according to the procedure in Ref. [7], where the nuclear breakup component on the Pb target was estimated from the measured C target cross section and was subtracted. The cross sections obtained here, for both targets, are slightly higher than those of Ref. [7] due to an improved analysis, taking into consideration the reaction loss of beam flux in the thick reaction targets, according to Eq. (1) of Ref. [24]. These small cross section differences are within the stated experimental uncertainties, and do not affect the conclusions of Ref. [7].

We now examine the γ-ray tagged partial cross sections. Doppler-shift-corrected γ-ray spectra in coincidence with ^{30}Ne residues for the C and Pb targets are shown in Fig. 1. The velocity of ^{30}Ne, for the Doppler correction, is deduced from the momentum of ^{30}Ne at the ZDS. The energy loss in the target is taken into consideration. A peak near 800 keV, corresponding to the $2_1^+ \rightarrow 0_1^+$ (ground-state) transition [27–29], is clearly observed for both C and Pb targets.

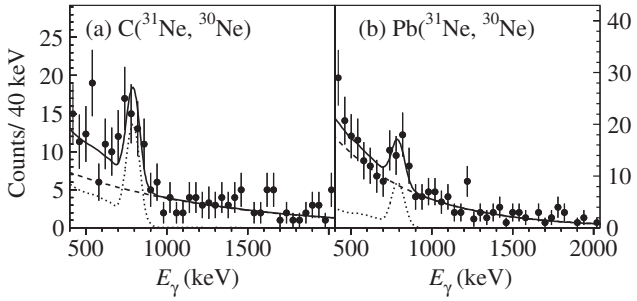

FIG. 1. γ-ray spectra of ^{30}Ne for the $1n$-removal of ^{31}Ne on (a) C, and (b) Pb targets. Deexcitation of the 2_1^+ state at $E_x \approx 800$ keV is observed in both cases. The fits to the spectra (solid curves) comprise the decay peak (dotted curves) on top of an exponential background (dashed curves).

With the energy of this transition fixed at 791 keV [27], the spectra are fitted with the detector response to this transition, obtained by a GEANT4 simulation, plus an exponentially falling background. The cross sections obtained from this transition are shown in the second row of Table I.

The partial cross sections for direct feeding of $^{30}\mathrm{Ne}(0_1^+)$ were obtained by subtracting those for the $2_1^+ \to 0_1^+$ γ-ray transition from the inclusive cross sections, under the assumption that all populated bound excited states above the 2_1^+ feed the ground state via the 2_1^+ state. These ground-state partial cross sections are shown in the last row of Table I. We note that the direct ^{30}Ne ground-state population dominates the Coulomb breakup cross section [85(23)%], but makes a lesser contribution [37(17)%] to the $1n$-removal cross section for the C target. This highlights the different sensitivity of the two reaction mechanisms to the removed neutron's wave function in ^{31}Ne.

We assume that the ^{30}Ne residues or cores are spectators whose initial states are not dynamically coupled in the fast collisions. Each $^{30}\mathrm{Ne}(J^\pi)$ residue is then associated with specific ^{31}Ne configurations, through the single-neutron overlaps $\langle {}^{30}\mathrm{Ne}(J^\pi)|{}^{31}\mathrm{Ne}\rangle$. For example, for a $^{31}\mathrm{Ne}(3/2^-)$ to $^{30}\mathrm{Ne}(0_1^+)$ transition, reactions are uniquely associated with $^{30}\mathrm{Ne}(0_1^+) \otimes \nu p_{3/2}$ configurations in ^{31}Ne. The distinct C and Pb target reaction sensitivities then enable one to examine the separation energy S_n and spectroscopic factor $C^2S(0_1^+; n\ell j)$ of the $^{30}\mathrm{Ne}(0_1^+)$ configuration. For excited final states of the residue, with $J^\pi \neq 0^+$, there can be several neutron configurations that contribute: e.g., $\nu p_{3/2}$, $\nu p_{1/2}$, $\nu f_{5/2}$, and $\nu f_{7/2}$ are possible for a $^{31}\mathrm{Ne}(3/2^-)$ to $^{30}\mathrm{Ne}(2_1^+)$ transition.

The $^{30}\mathrm{Ne}(0_1^+)$ partial cross section on the C target, $\sigma_{-1n}(\mathrm{C}; 0_1^+) = 33(15)$ mb, and its Coulomb breakup cross section on the Pb target, $\sigma_{-1n}(E1; 0_1^+) = 448(108)$ mb, can now be compared with the calculated single-particle cross sections $\sigma_{\mathrm{SP}}(\mathrm{C}; n\ell j)$ and $\sigma_{\mathrm{SP}}(E1; n\ell j)$, computed for a unit C^2S. We construct the required neutron single-particle wave functions as eigenstates of Woods-Saxon potentials with geometry parameters (r_0, $a_0 = 0.7$ fm) and a fixed spin-orbit potential of strength $V_{\mathrm{SO}} = 6.0$ MeV. For the sd-shell orbitals the r_0, constrained by spherical Hartree-Fock calculations [30], are 1.119 ($2s_{1/2}$), 1.203 ($1d_{5/2}$), and 1.231 ($1d_{3/2}$) fm. For the fp-shell orbitals we take $r_0 = 1.25$ fm. The potential depths for each $n\ell j$ are adjusted to reproduce the physical separation energy. The $\sigma_{\mathrm{SP}}(\mathrm{C}; n\ell j)$ values are given by the eikonal-model calculations [24,31], and the $\sigma_{\mathrm{SP}}(E1; n\ell j)$ by direct breakup calculations [7], with distinct sensitivities to S_n.

Figure 2 shows, as a function of the assumed S_n and J^π of the ^{31}Ne ground state, the two independent $C^2S(0_1^+; n\ell j)$ values deduced from the cross section ratios $\sigma_{-1n}(C; 0_1^+)/\sigma_{\mathrm{SP}}(\mathrm{C}; n\ell j)$ and $\sigma_{-1n}(E1; 0_1^+)/\sigma_{\mathrm{SP}}(E1; n\ell j)$. The blue (red) shaded regions result from the C target (Coulomb breakup) data. The deduced $C^2S(0_1^+; n\ell j)$ and S_n consistent with

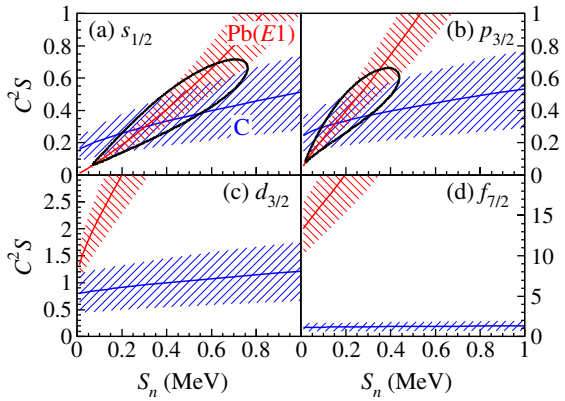

FIG. 2 (color online). Deduced spectroscopic factors C^2S from the $^{30}\mathrm{Ne}(0_1^+)$ partial cross section on the C target and Coulomb breakup on the Pb target as a function of the assumed S_n and J^π of ^{31}Ne. Calculations are shown for (a) $1/2^+$: $^{30}\mathrm{Ne}(0_1^+) \otimes 2s_{1/2}$; (b) $3/2^-$: $^{30}\mathrm{Ne}(0_1^+) \otimes 2p_{3/2}$; (c) $3/2^+$: $^{30}\mathrm{Ne}(0_1^+) \otimes 1d_{3/2}$; and (d) $7/2^-$: $^{30}\mathrm{Ne}(0_1^+) \otimes 1f_{7/2}$. The $1/2^+$ and $3/2^-$ cases have overlap between the results of the two reaction mechanisms, delimited by the solid lines (1σ limit).

the measured cross sections and the stated reaction models are represented by their region of overlap, delimited by solid lines showing the 1σ limit (68% confidence level). It is shown that $J^\pi = 3/2^+$ and $7/2^-$ ground-state spin assignments for ^{31}Ne lead to no such overlap, but both $J^\pi = 1/2^+$ and $3/2^-$ assignments do, limiting the J^π to the latter possibilities with low-ℓ (s- or p-wave) orbitals. Figure 2 determines, for $J^\pi = 1/2^+$, $S_n = 0.30^{+0.26}_{-0.17}$ MeV and $C^2S(0_1^+; 2s_{1/2}) = 0.30^{+0.25}_{-0.17}$, and for $J^\pi = 3/2^-$, $S_n = 0.15^{+0.16}_{-0.10}$ MeV and $C^2S(0_1^+; 2p_{3/2}) = 0.32^{+0.21}_{-0.17}$. These S_n values are consistent with reported limits [20].

To further disentangle these s-wave ($1/2^+$) or p-wave ($3/2^-$) possibilities, we compare the experimental inclusive and partial $1n$-removal cross sections on the C target with those obtained using eikonal-model calculations and shell-model C^2S values. We adopt two sets of SM calculations: SM(i) uses the Warburton-Becker-Millener-Brown (WBMB) interaction, with $2\hbar\omega$ sd-pf cross-shell excitations allowed [32], while SM(ii) uses the modified monopole, sd-pf cross-shell (SDPF-M) interaction and exploits recently developed, exact diagonalization techniques, and allows any number of cross-shell excitations among sd and $1f_{7/2}2p_{3/2}$ orbitals [33]. These represent plausible models for ^{31}Ne and describe the observed low-lying spectra of ^{30}Ne [28,29] and ^{32}Ne [28] to within about 300 keV. Other SM calculations, such as those of Ref. [34], are not considered, as their smaller model space results in $C^2S(0_1^+; 2s_{1/2}) = 0$ and precludes the $J^\pi = 1/2^+$ ground-state configuration of interest here.

A precis of results is shown in Table II. All predicted SM configurations and transitions to bound ^{30}Ne excited states were included in the inclusive cross sections. Both the inclusive and $^{30}\mathrm{Ne}(0_1^+)$ partial cross sections are

TABLE II. Experimental partial and inclusive $1n$-removal cross sections [σ_{-1n}(C)] are compared with eikonal-model calculations [$\sigma^{\rm th}_{-1n}$(C)] using C^2S values from the SM(i) and SM(ii) calculations. The upper part is for a ^{31}Ne($3/2^-$) ground-state assignment, and the lower part is for a $1/2^+$ assignment. Calculated partial cross sections leading to excited ^{30}Ne states (^{30}Ne*) with positive parities are also shown.

Shell-model configuration	σ_{-1n}(C) (mb)	SM(i) C^2S	WBMB $\sigma^{\rm th}_{-1n}$(C) (mb)	SM(ii) C^2S	SDPF-M $\sigma^{\rm th}_{-1n}$(C) (mb)
C(^{31}Ne($3/2^-$), ^{30}Ne)					
^{30}Ne(0^+_1) $\otimes$ $2p_{3/2}$	33(15)	0.080	9.2	0.21	24.3
^{30}Ne* $\otimes$ $2p_{3/2}$		0.21	14.4	0.34	21.4
^{30}Ne* $\otimes$ $1f_{7/2}$		1.36	32.9	0.80	18.8
Inclusive	90(7)		58.3		93.3
C(^{31}Ne($1/2^+$), ^{30}Ne)					
^{30}Ne(0^+_1) $\otimes$ $2s_{1/2}$	33(15)	0.011	1.3	0.011	1.3
^{30}Ne* $\otimes$ $1d_{3/2}$		0.76	16.2	0.55	12.8
Inclusive	90(7)		18.1		51.1

consistent with the $J^\pi = 3/2^-$ assignment and the C^2S values of SM(ii), while they are not reproduced for $1/2^+$ with either of the SM calculations. The ratio σ_{-1n}(C):$\sigma^{\rm th}_{-1n}$(C) for the $3/2^-$ assignment and SM(ii) is consistent with unity and with the $1n$-removal reaction systematics for weakly bound nuclei [30]. This comparison indicates that the ^{31}Ne ground state has spin-parity $3/2^-$.

The larger $2p_{3/2}$ C^2S values from SM(ii) in Table II reflect the near-degenerate $1f_{7/2}$ and $2p_{3/2}$ effective single-particle energies arising from the SDPF-M interactions [33]. The SM(ii) cross-shell excitations show larger $p_{3/2}$ occupancy than for SM(i), and the larger p-shell C^2S, required by the current data, support these features of the SM(ii) calculation.

Figure 3 now shows the inclusive $1n$-removal parallel momentum distribution of ^{30}Ne residues, in the ^{31}Ne c.m. frame, for reactions on the C target. The width of the momentum distribution is 77(18) MeV/c, extracted from a Lorentzian fit. Such a narrow width is another signature of a sizable $1n$ halo component in ^{31}Ne. The measured distribution is also consistent with the eikonal calculations using the C^2S values of SM(ii) [Fig. 3(a), (ii)]. It is not reproduced when using either the $J^\pi = 3/2^-$ C^2S values of SM(i) [Fig. 3(a), (i)] or when assuming a $1/2^+$ assignment [Fig. 3(b)], adding strength to the $3/2^-$ assignment. The consistency of the observed momentum distribution, inclusive, and partial cross sections with the SM(ii) spectroscopy suggests that the ^{31}Ne ground state is well described by these predicted SM configurations. The levels spectrum of this SM calculation also supports the $3/2^-$ ground state, with the lowest $1/2^+$ state being predicted as the fifth excited state at 0.99 MeV: above $5/2^-$(0.42 MeV), $7/2^-$(0.48 MeV), $3/2^-_2$(0.63 MeV), and $3/2^+$(0.65 MeV) excited states.

These key results are, therefore, that the ^{31}Ne ground state has $J^\pi = 3/2^-$, $C^2S(0^+_1; 2p_{3/2}) = 0.32^{+0.21}_{-0.17}$, and $S_n = 0.15^{+0.16}_{-0.10}$ MeV, the smallest S_n of any known neutron-rich nucleus. Thus, the ^{31}Ne halo component is formed of an extremely weakly bound p-wave neutron that carries only about 30% of a single-nucleon strength. This reduced halo strength suggests a large degree of configuration mixing of the fp orbitals in the ^{31}Ne ground state, a signature of deformation.

We now elucidate this deformation property of ^{31}Ne with reference to the SM(ii) calculations. These predict a large intrinsic electric quadrupole moment $Q_0 \approx 60$ fm^2, corresponding to the quadrupole deformation parameter $\beta \approx 0.56$. This Q_0 value was extracted from both the calculated static quadrupole moment, $Q = 12.3$ fm^2, and the reduced $E2$ transition probability, $B(E2) = 93.3e^2$ fm^4, from the ground state to the predicted $7/2^-_1$ state. There is remarkable agreement between the Q_0 values from these independent estimates. Thus, in addition to the ($C^2S \approx 0.3$) p-wave neutron halo component in the ground state, ^{31}Ne is strongly deformed as a whole. Such a feature is in contrast to the light s-wave $1n$ halo in ^{11}Be and ^{19}C that carries about 70% of the single-nucleon strength [8–13], where the halo itself is spherical even though the core could be deformed.

Irrespective of this expected quadrupole collectivity of ^{31}Ne, $E2$ contributions to its Coulomb dissociation cross section are small for energies ≈230 MeV/nucleon. The summed $E2$-transition cross sections to the $5/2^-_1$ and $7/2^-_1$ ^{31}Ne excited states, as predicted by the SM(ii) calculations, with $B(E2)$ values of 169 and $93.3e^2$ fm^4, are estimated to

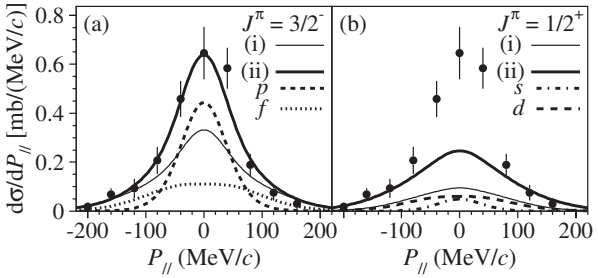

FIG. 3. Inclusive parallel momentum distribution of ^{30}Ne residues after $1n$ removal from ^{31}Ne on the C target, compared to eikonal-model predictions using C^2S values of calculations SM(i) and SM(ii) for (a) $J^\pi = 3/2^-$ and (b) $J^\pi = 1/2^+$. The valence neutron contributions from p and f waves, for $3/2^-$, and from s and d waves, for $1/2^+$, for SM(ii) are also shown.

be ≈42 mb [35]. This ≈10% contribution to the calculated Pb target cross section has a very minor effect on the results presented.

The deformation of ^{31}Ne has also been discussed in terms of the Nilsson model. Hamamoto showed that ^{31}Ne, with a $3/2^-$ ground state, can be described by the Nilsson orbitals $[330]1/2$, for $0.22 \leq \beta \leq 0.30$, and $[321]3/2$, for $0.40 \leq \beta \leq 0.59$ [36]. The latter corresponds to a $3p$-$2h$ configuration, a dominant one in the SM(ii) calculation that predicts a similar β value. It is noted that the p-wave component becomes relatively more significant than the f-wave component as S_n approaches zero [18,19]. Recent calculations using the particle-rotor model [37] and the antisymmetrized molecular dynamics approach [38] also propose that ^{31}Ne is strongly deformed with $J^\pi = 3/2^-$.

The shell and Nilsson models mentioned above suggest that the near degeneracy of orbitals of the same parity, the $p_{3/2}$ and $f_{7/2}$ single-particle orbitals, can drive large quadrupole deformation due to the nuclear Jahn-Teller effect [16,39,40]. Such large deformation is consistent with the picture of ^{31}Ne as a member of the island of inversion nuclei and is in line with the mixing and fragmentation of configurations. The near degeneracy of the fp orbitals can also be explained by mean-field calculations [15,16], reflecting the different rate at which each single-particle orbital migrates as one approaches the weak binding limit.

Also of note is that the Jahn-Teller effect driven quadrupole deformation, from the near degeneracy of the fp orbital, leads the lowest three Nilsson orbitals, $[330]1/2$, $[321]3/2$, and $[321]1/2$, to the $3/2^-$ ground state. Such p-wave importance suggests that neutron drip line nuclei with $N = 21$, 23, and 25 may also exhibit significant deformed p-wave $1n$-halo components. ^{31}Ne is considered a prototype of such cases. The study of p-wave halo components in ^{37}Mg will be interesting to explore these phenomena. This onset of deformation due to the degeneracy of adjacent single-particle states of the same parity is expected to occur in heavier neutron-rich nuclei [16]. Such deformed halo components could thus be a common feature in nuclei along the neutron drip line toward medium mass, which may enhance our understanding of nuclear stability at the limits of weak binding. For ^{31}Ne, more complete data should further clarify the deformation properties discussed, in particular, of the quadrupole moment, rotational levels, and their transitions.

We wish to extend our thanks to the accelerator staff of the RIKEN Nishina Center for their efforts in delivering the intense ^{48}Ca beam. Fruitful discussions with I. Hamamoto are greatly appreciated. This work was supported in part by JSPS KAKENHI Grant No. 22340053 and MEXT KAKENHI Grant No. 24105005. N. K. acknowledges the Grant-in-Aid support by JSPS (No. 25·10601). J. A. T. acknowledges support of the Science and Technology Facilities Council (U.K.) Grant No. ST/J000051.

[1] I. Tanihata, Prog. Part. Nucl. Phys. **35**, 505 (1995).
[2] A. S. Jensen, K. Riisager, D. V. Fedorov, and E. Garrido, Rev. Mod. Phys. **76**, 215 (2004).
[3] B. Jonson, Phys. Rep. **389**, 1 (2004).
[4] T. Frederico, A. Delfino, L. Tomio, and M. T. Yamashita, Prog. Part. Nucl. Phys. **67**, 939 (2012).
[5] I. Tanihata, H. Savajols, and R. Kanungo, Prog. Part. Nucl. Phys. **68**, 215 (2013).
[6] M. Takechi *et al.*, Phys. Lett. B **707**, 357 (2012).
[7] T. Nakamura *et al.*, Phys. Rev. Lett. **103**, 262501 (2009).
[8] T. Nakamura *et al.*, Phys. Lett. B **331**, 296 (1994); N. Fukuda *et al.*, Phys. Rev. C **70**, 054606 (2004).
[9] R. Palit *et al.*, Phys. Rev. C **68**, 034318 (2003).
[10] S. Fortier *et al.*, Phys. Lett. B **461**, 22 (1999).
[11] T. Aumann *et al.*, Phys. Rev. Lett. **84**, 35 (2000).
[12] K. T. Schmitt *et al.*, Phys. Rev. Lett. **108**, 192701 (2012).
[13] T. Nakamura *et al.*, Phys. Rev. Lett. **83**, 1112 (1999).
[14] V. Rotival and T. Duguet, Phys. Rev. C **79**, 054308 (2009).
[15] I. Hamamoto, Phys. Rev. C **76**, 054319 (2007).
[16] I. Hamamoto, Phys. Rev. C **85**, 064329 (2012).
[17] Y. Utsuno, T. Otsuka, B. A. Brown, M. Honma, T. Mizusaki, and N. Shimizu, Phys. Rev. C **86**, 051301(R) (2012).
[18] T. Misu, W. Nazarewicz, and S. Åberg, Nucl. Phys. **A614**, 44 (1997).
[19] I. Hamamoto, Phys. Rev. C **69**, 041306(R) (2004).
[20] L. Gaudefroy *et al.*, Phys. Rev. Lett. **109**, 202503 (2012).
[21] P. G. Hansen, and J. A. Tostevin, Annu. Rev. Nucl. Part. Sci. **53**, 219 (2003).
[22] T. Aumann and T. Nakamura, Phys. Scr. **T152**, 014012 (2013).
[23] V. Maddalena *et al.*, Phys. Rev. C **63**, 024613 (2001).
[24] N. Kobayashi *et al.*, Phys. Rev. C **86**, 054604 (2012).
[25] T. Kubo, Nucl. Instrum. Methods Phys. Res., Sect. B **204**, 97 (2003).
[26] T. Ohnishi *et al.*, J. Phys. Soc. Jpn. **77**, 083201 (2008).
[27] Y. Yanagisawa *et al.*, Phys. Lett. B **566**, 84 (2003).
[28] P. Doornenbal *et al.*, Phys. Rev. Lett. **103**, 032501 (2009).
[29] P. Fallon *et al.*, Phys. Rev. C **81**, 041302(R) (2010).
[30] A. Gade *et al.*, Phys. Rev. C **77**, 044306 (2008).
[31] E. C. Simpson and J. A. Tostevin, Phys. Rev. C **79**, 024616 (2009).
[32] E. K. Warburton, J. A. Becker, and B. A. Brown, Phys. Rev. C **41**, 1147 (1990).
[33] Y. Utsuno, T. Otsuka, T. Mizusaki, and M. Honma, Phys. Rev. C **60**, 054315 (1999).
[34] A. Poves and J. Retamosa, Nucl. Phys. **A571**, 221 (1994).
[35] C. A. Bertulani, C. M. Campbell, and T. Glasmacher, Comput. Phys. Commun. **152**, 317 (2003).
[36] I. Hamamoto, Phys. Rev. C **81**, 021304(R) (2010).
[37] Y. Urata, K. Hagino, and H. Sagawa, Phys. Rev. C **83**, 041303(R) (2011).
[38] K. Minomo, T. Sumi, M. Kimura, K. Ogata, Y. R. Shimizu, and M. Yahiro, Phys. Rev. Lett. **108**, 052503 (2012).
[39] H. A. Jahn and E. Teller, Proc. R. Soc. A **161**, 220 (1937).
[40] P.-G. Reinhard and E. W. Otten, Nucl. Phys. **A420**, 173 (1984).